# Abrikosov vortex corrections to effective magnetic field enhancement in epitaxial graphene

Luke R. St. Marie, Chieh-I Liu, I-Fan Hu, Heather M. Hill, Dipanjan Saha, Randolph E. Elmquist, Chi-Te Liang, David B. Newell, Paola Barbara, Joseph A. Hagmann, and Albert F. Rigosi

# Abrikosov vortex corrections to effective magnetic field enhancement in epitaxial graphene

Luke R. St. Marie,[1,2] Chieh-I Liu,[1,3] I-Fan Hu,[1,4] Heather M. Hill,[1] Dipanjan Saha,[1] Randolph E. Elmquist,[1] Chi-Te Liang,[2] David B. Newell,[1] Paola Barbara,[2] Joseph A. Hagmann,[1] and Albert F. Rigosi[1*]

[1]*Physical Measurement Laboratory, National Institute of Standards and Technology (NIST), Gaithersburg, MD 20899, USA*

[2]*Department of Physics, Georgetown University, Washington, District of Columbia 20057, USA*

[3]*Department of Chemistry and Biochemistry, University of Maryland, College Park, Maryland 20742, USA*

[4]*Department of Physics, National Taiwan University, Taipei 10617, Taiwan*

ABSTRACT: Here we report the effects of enhanced magnetic fields resulting from type II superconducting NbTiN slabs adjacent to narrow Hall bar devices fabricated from epitaxial graphene. Observed changes in the magnetoresistances were found to have minimal contributions from device inhomogeneities, magnet hysteresis, electron density variations along the devices, and transient phenomena. We hypothesize that Abrikosov vortices, present in type II superconductors, contribute to these observations. By determining the London penetration depth, coupled with elements of Ginzburg-Landau theory, one can approximate an upper bound on the effect that vortex densities at low fields (below 1 T) have on the reported observations. These analyses offer insights into device fabrication and how to utilize the Meissner effect for any low-field and low-temperature applications using superconductors.

---

[*] Email: albert.rigosi@nist.gov

# I. INTRODUCTION

Graphene has proven, in the last decade, to be a technologically useful material thanks to its extraordinary electrical properties [1-4]. Its low-field (less than 3 T) transport applications are far-reaching, ranging from spintronics devices [5-7], to electron optics [8-11], to serving as a standard for resistance [12-16]. Moreover, graphene continues to offer research avenues in the lower-field regime, where its physics may be studied and implemented for the discovery and optimization of nanoscale and macroscopic devices.

One of the frequent requirements for measuring graphene-based devices for the transport applications listed above is the use of a magnetic field ($B$-field) to activate or reveal certain effects. For low-field applications, commercially available permanent magnets can only exhibit a field as strong as 1 T. Such a limit could benefit from potential magnetic enhancement provided by the device being used. The Meissner effect in type I superconductors could deliver significant enhancement in local areas due to B-field screening, but with the major disadvantage that all of these superconductors have critical fields well below 1 T. Consequently, for many practical applications, type II superconductors provide more flexibility. Many efforts have been concerned with direct interactions of superconductors on or around graphene in the form of proximity effects, Andreev reflections, and device contacting [17-20], but fewer efforts report information on the extent to which $B$-fields could be enhanced with superconductors [21-22].

In this work, we investigate the effects of adjacent type II superconducting NbTiN slabs on the measured resistances of narrow Hall bar devices fabricated from epitaxial graphene on 4H-SiC. Observed apparent changes in the magnetoresistances, and by extension, the electron densities, suggest that the devices are experiencing an enhanced $B$-field, whose transverse profile is

analyzed in the context of the Meissner effect and Abrikosov vortices in type II superconductors. The upper critical $B$-field for the NbTiN slabs was determined with experimental data, enabling one to determine the London penetration depth ($\lambda_L$). When coupled with elements of Ginzburg-Landau theory, an approximation of the vortex densities in the low-field regime was calculable. The results and analyses presented here offer advancement in the application space of low-field, low-temperature technologies, where the local $B$-field enhancement is able to reduce future $B$-field requirements for a variety of devices.

## II. EXPERIMENTAL AND NUMERICAL METHODS

### A. Device Preparation

Epitaxial graphene (EG) films were grown on 4H-SiC substrates at a temperature of 1900 °C. This temperature enables Si atoms to sublimate from the substrate, allowing C atoms to form a hexagonal lattice. Substrates were diced from 4H-SiC(0001) wafers from CREE [23] and chemically cleaned with a 5:1 diluted solution of hydrofluoric acid and deionized water. Substrates were then processed with AZ5214E to utilize polymer-assisted sublimation [24]. Next, substrates were placed on a polished graphite slab (SPI Glas 22 [23]) silicon-face down. The growth furnace was flushed with argon gas and filled (100 kPa) from a 99.999 % liquid argon source. The graphite-lined resistive-element furnace (Materials Research Furnaces Inc. [23]) was held at 1900 °C for approximately 5 min, with respective heating and cooling rates of about 1.5 °C/s.

Following the completion of the epitaxial growth procedure, EG films were inspected with optical and confocal laser scanning microscopy, as described by previous work [25]. For device fabrication, we followed well-documented photolithography processes designed for etching Hall

bars and corresponding device contacts [26], using a layer of Pd/Au to protect the EG surface from organic contaminants. A key difference in our process was the use of NbTiN for the contact pad material, a decision made on the basis of this material's superconducting properties [27-28]. A control device design is illustrated in Fig. 1 (a), with the injected current intended to travel across the length of the device and the four pairs of orthogonal contacts intended for Hall resistance measurements. Before removing the protective Pd/Au layer from the EG, 1-μm-thick superconducting slabs composed of NbTiN were deposited on each side of the graphene Hall bar (150 μm wide, along various lengths), as illustrated in Fig. 1 (b) and seen in final form in Fig. 1 (c). Externally applied $B$-fields between the lower and upper critical $B$-fields of NbTiN are expected to deform around the slabs as magnetic flux incrementally penetrates the slab in the form of Abrikosov vortices, with the potential for flux pinning to occur due to impurities and disorder [29-31].

The last step for device preparation was the functionalization process to regulate the electron density without the need for a top gate. The compound $Cr(CO)_6$ was used in a custom, nitrogen-filled furnace at 130 °C. At this temperature, the compound breaks down and forms functional group $Cr(CO)_3$, which bonds to the EG surface in a way that does not degrade the electrical properties [32-35]. This step is crucial because it allows the electron density to remain low (on the order $10^{10}$ cm$^{-2}$) while stored in air, and with uniform annealing, supports a uniform electron density across the device. The variation across the entire chip is on the order of $10^{10}$ cm$^{-2}$ [34], which is small compared to the typical values of inherent electron doping in EG of $10^{13}$ cm$^{-2}$ [36]. The EG surface also typically hosts harmless particulates of oxidized chromium.
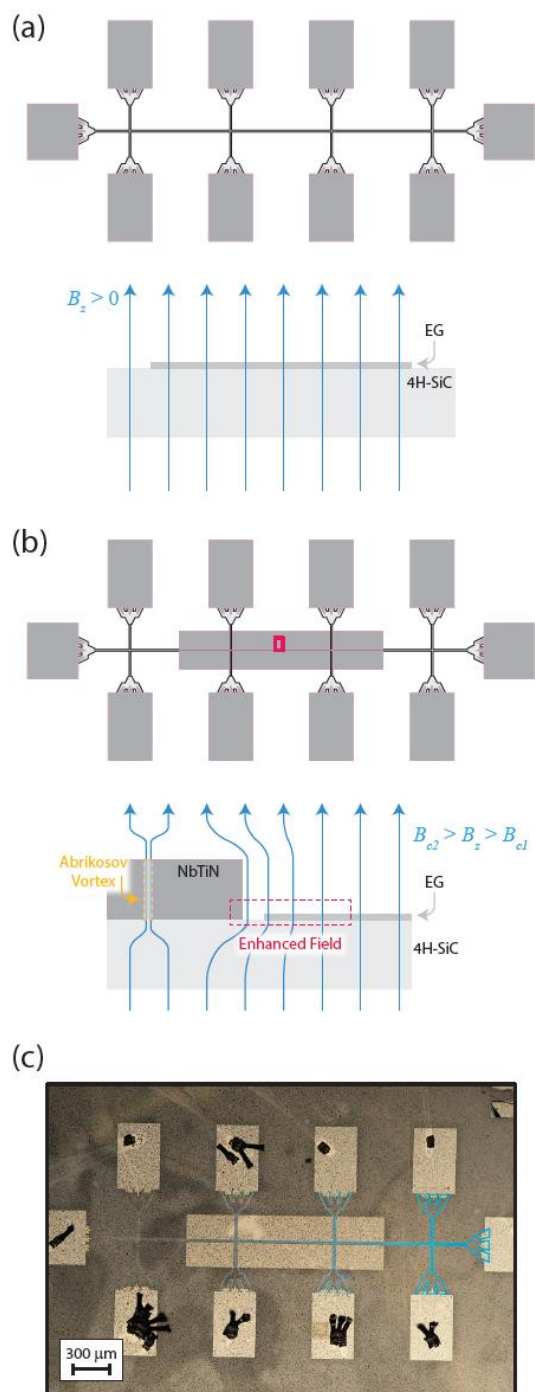
FIG. 1. (Color online) (a) An illustration of the control device is provided. The length and width of the Hall bar device are approximately 2 mm and 10 μm, respectively. A cross-section is shown below, and under normal applied $B$-fields, field lines do not deviate. (b) An illustration of the device with the superconducting slabs is provided. The small red region indicates a magnification and cross-section shown just below. Along the top edge of the Hall bar within the

regions surrounded by adjacent NbTiN slabs, the *B*-field is expected to deform as a result of the type II superconducting mixed state (lines represent *B*-field, not flux quanta). (c) The optical image shows an example device that was measured, with a gradually fading light blue augmented outline showing the perimeter of the etched EG. The appearance of dirt or residue is a result of the functionalization process.

## B. Device and Superconductor Characterization

A Janis Cryogenics cryostat was utilized for transport measurements [23]. All relevant data were collected at *B*-field values between 0 T and ±5 T, and at temperatures within the range 1.5 K to 15 K and currents as high as 22 µA. Data from Hall resistance and longitudinal resistivity measurements were collected with lock-in amplifiers. The superconducting NbTiN slabs were characterized to determine several parameters beneficial for later analyses. The spacing between the slab edge and the EG edge was designed to be 5 µm. In Fig. 2 (a), the NbTiN slab resistance was measured as a function of temperature using 1 µA of applied current, with the transition temperature determined to be about 12.51 K by taking the midpoint between the 10 % and 90 % asymptotic normal-state resistance values.

Additional data on the upper critical field of the NbTiN slab are provided in the Supplemental Material [37]. In short, the approximation $B_{c2}(0) \approx 0.69 \, T_c \frac{dB_{c2}}{dT}$ gives us an upper critical field (at 0 K) of 11.41 T ± 1.02 T [38-39]. With the well-known condition of overlapping vortices occurring at the upper critical field in type II superconductors, $B_{c2} = \frac{\Phi_0}{2\pi\xi^2}$, one may determine the coherence length $\xi$ = 5.37 nm ± 0.24 nm. Given its relevance in later analyses, $\lambda_L$ was determined by taking the reported value in the literature of the depairing current density in NbTiN [40-42]:

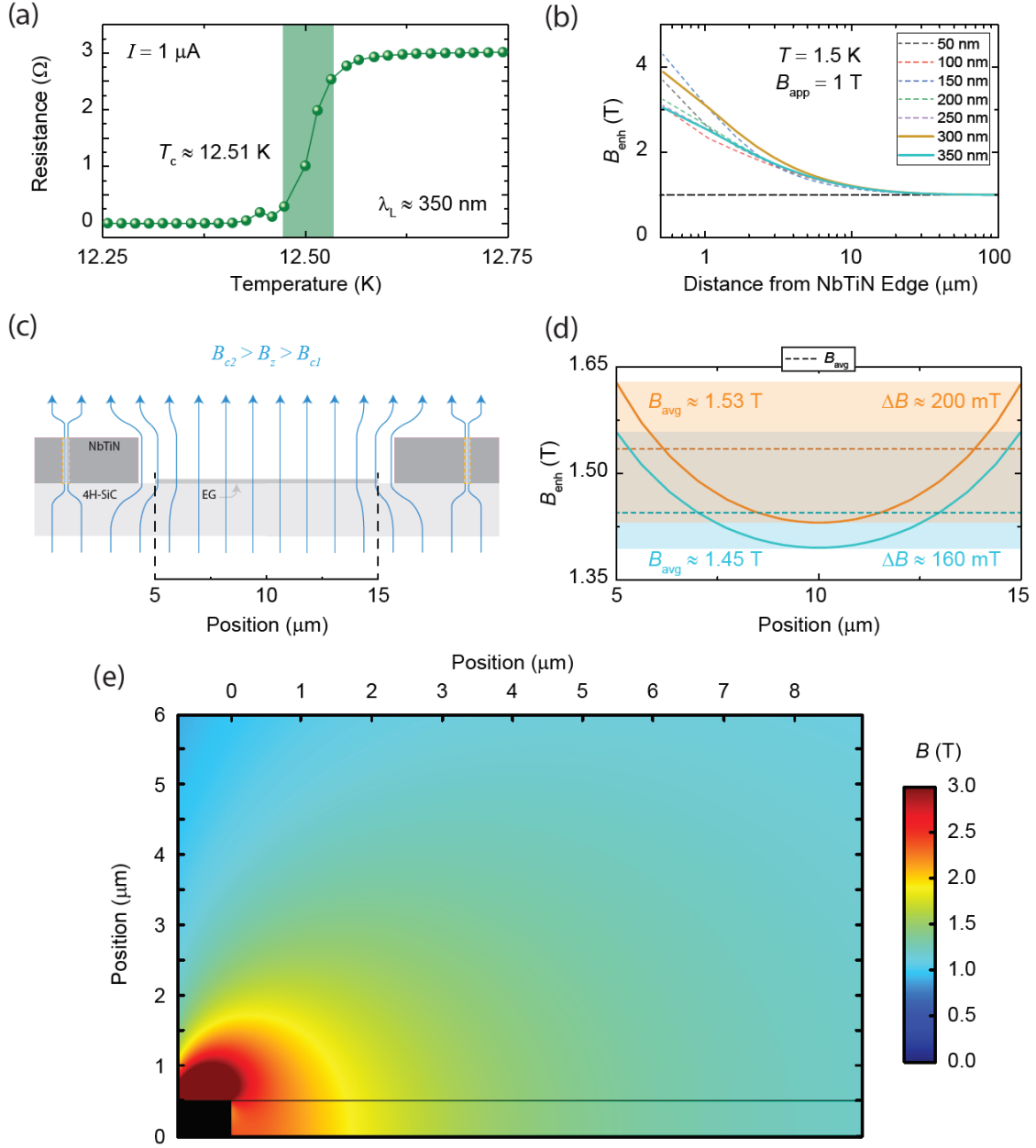$$J_d(0) = \sqrt{\frac{2\Phi_0 B_{c2}(0)}{27\pi\mu_0^2 \lambda_L^{\,4}(0)}}$$

(1)



FIG. 2. (Color online) (a) The NbTiN slab resistance was measured as a function of temperature using 1 μA, with the transition temperature determined to be approximately 12.5 K. (b) COMSOL simulations show the enhanced *B*-field drop off away from the slab for different values of $\lambda_L$ [23]. Simulations were performed at 1.5 K and 1 T. The two solid lines indicate the

closer approximations to the determined $\lambda_L$. (c) An illustration of the *B*-field enhancement along the width of the device is provided, with the corresponding *B*-field profile shown in (d). (d) The *B*-field profiles for two $\lambda_L$ (300 nm and 350 nm, in orange and light blue color themes, respectively) were simulated along the width of the device, giving an idea for the range of *B*-field variation and the average enhanced field. (e) A color map of the simulated enhanced *B*-field along the cross-section of the device (dashed red box in Fig. 2 (b)) was generated with COMSOL at 1 T, with the black box in the lower left corner indicating the end of the NbTiN slab and the EG film aligned with the bottom horizontal axis (starting at 5 μm) [23].

Using the reported $J_d(0) = 1.5 \times 10^{11}\,{}^A\!/_{m^2}$ and $\Phi_0$ (2.0678 × 10$^{-15}$ Wb), our $\lambda_L(0) \approx$ 354 nm $\pm$ 8 nm. This value does not change significantly at our measurement temperature of 1.5 K since this is an order of magnitude below the NbTiN transition temperature. It thus follows that the approximate Ginzburg-Landau parameter $\kappa = \frac{\lambda}{\xi} \approx 66$.

## C.  COMSOL Simulations

The cross-platform finite element analysis software COMSOL was employed for simulating the Meissner effect in NbTiN [23]. The model was constructed with cylindrical symmetry to prevent the complications that can occur in rectangular coordinates [43-44]. The layout may be seen in the Supplemental Material [37]. The applied *B*-field for the simulations was 1 T and assumed a perfect Meissner state in NbTiN. The component values in the calculated *B*-field vector array scale linearly with applied *B*-field. The enhanced *B*-field strength along the direction away from the slab is shown in Fig. 2 (b) as a function of distance for various $\lambda_L$. The two solid lines indicate the closer approximations to the determined $\lambda_L$. The drop-off of the magnetic field strength away from the NbTiN is approximately proportional to the reciprocal distance cubed, as can be found from a log-log plot of Fig. 2 (b) and comparing with similar calculations [45].

An illustration and corresponding $B$-field enhancement is shown for the cross-section of the device in Fig. 2 (c) and (d), respectively. For the cases of $\lambda_L$ being approximately 300 nm (orange colors) or 350 nm (light blue colors), the average $B$-fields were 1.53 T and 1.45 T, respectively and as indicated by the dotted lines, with corresponding variations of 200 mT and 160 mT. In Fig. 2 (e), a color map of the enhanced $B$-field in the cross-sectional area of the device edge was generated. Note that the horizontal axis origin starts at the slab edge (and the EG film at 5 μm on the horizontal axis and 0 μm on the vertical axis), whereas the vertical axis starts in the center of the slab.

### III. OBSERVATION OF APPARENT MAGNETIC FIELD ENHANCEMENT

Transport measurements were performed on control and experimental devices, exemplified by the illustrations in Fig. 3 (a) and (b), respectively. In the control device, Hall resistances were measured in four regions, indicated by the black, red, green, and blue curves. The slope of the Hall resistance at low-field (less than 1 T) was used to calculate the electron density: $n_e = \frac{1}{e\left(\frac{dR_{xy}}{dB}\right)}$. The variation in the electron density is within the expected behavior, namely on the order of $10^{10}$ cm$^{-2}$ [34]. Corresponding longitudinal resistance data were also collected. In Fig. 3 (b), a device with the NbTiN slabs had the same four regions measured. The presence of the NbTiN slabs is a key difference in the configuration for regions 2 and 3. For both sets of data, apparent horizontal scalings of the resistance curves were observed. All data were adjusted for magnet hysteresis (see the Supplemental Material [37]).

To better understand the forthcoming analysis of these data, a description of the physical phenomena behind all of these observations will be helpful. In the top data panel of Fig. 3 (a), four distinct Hall resistances were measured simultaneously on the control device. These data

appear to take on negative magnetoresistances because of the change in polarity of the *B*-field. Ultimately, the experimental measurements were recording the voltages between the top and bottom sets of electrical contacts. As with typical quantum Hall effect data, the $\nu = 2$ plateaus appear to be at $\pm\frac{h}{2e^2}$. The resistance data are obtained by dividing the measured voltages by the applied current, and since the voltages adopt a negative value for negative *B*-field values, one should expect to see the data as they appear in both $R_{xy}$ panels. For the data in the top panel of Fig. 3 (b), all four Hall resistances no longer overlap within expected electron density variations. Rather, the data for regions 1 and 4 (no adjacent slab) describe a similar electron density whereas the data for regions 2 and 3, though matching in shape, describe a device with a different electron density (determined by the slope at low field as seen above). For Fig. 3 (b), the device was adjusted so that data were acquired at a different electron density than in Fig. 3 (a) to accentuate the effects of the adjacent NbTiN slab. That is, at lower electron densities, the effect is still visible, but more susceptible to experimental error due to the natural electron density variation across the device [34].

By focusing on the bottom data panels of Fig. 3 (a) and (b), one may extract a similar conclusion with the measured longitudinal resistivities. The notable observation for the longitudinal resistivity is that, when measuring the voltage between two adjacent electrical contacts within the region near the NbTiN slab, the resulting resistivity also appears horizontally contracted (red and green curves of Fig. 3 (b)) with respect to a longitudinal resistivity determined outside of the effected regions. At lower electron densities, like that in Fig. 3 (a), the longitudinal resistivity remains subdued, having only a major peak near zero-field [34]. However, at higher electron densities, the emergence of Shubnikov-de-Haas oscillations becomes prominent, manifesting as side peaks in the magnetoresistance [46]. The electron

density may also be estimated from the periodicity of these oscillations, but such estimations are not as accurate in this case as those estimated from the linearity of the Hall response. A very rough estimate of the horizontal scaling factor for both the Hall resistance and longitudinal resistivity may be estimated by simple contraction of the horizontal axis for the data taken in the regions not adjacent to the NbTiN slab, and in this case is approximately 15 %. The question then becomes one of determining the cause of the observed scaling.
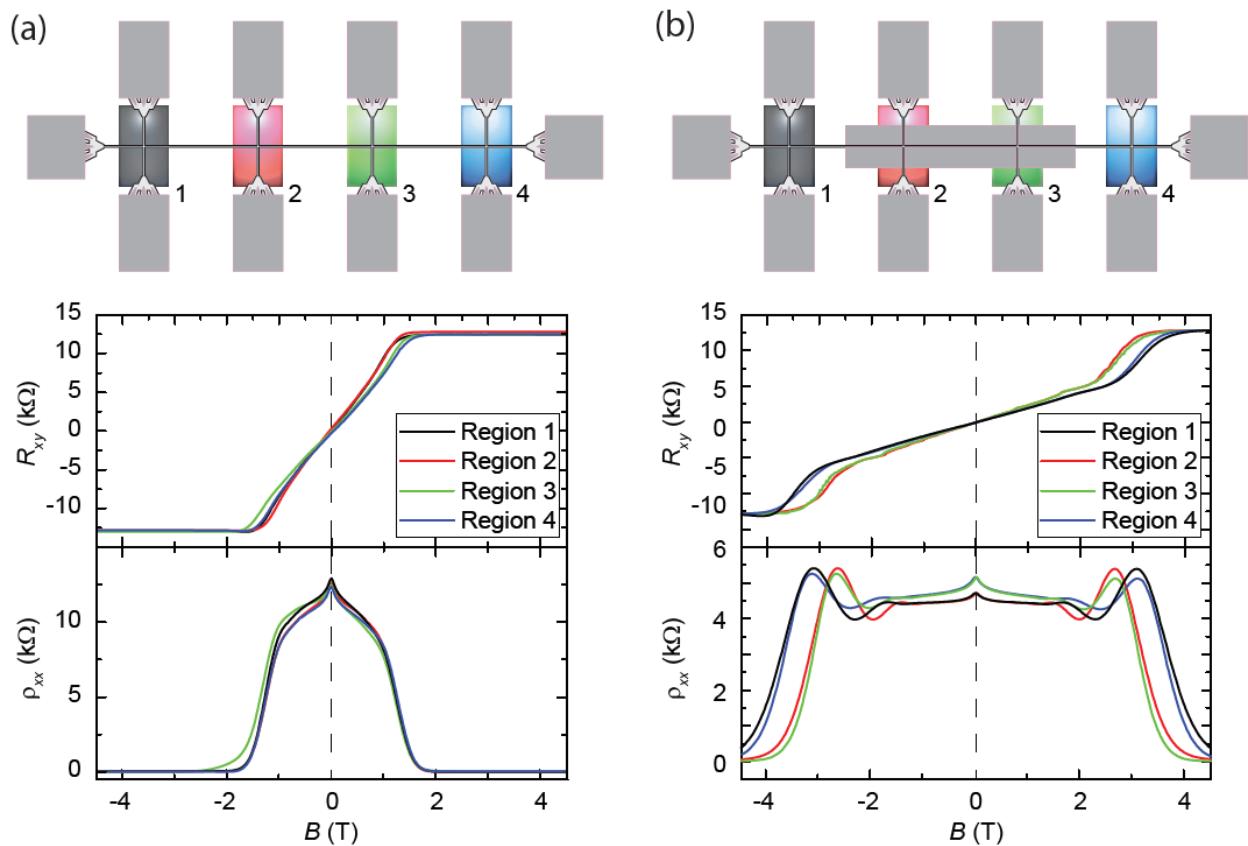


FIG. 3. (Color online) (a) In the control device (top panel), the Hall resistances were measured in four regions, indicated by the corresponding color themes. By extension, their electron densities were determined using the low-field slope to verify device uniformity. The bottom panel shows the longitudinal resistivity curves. (b) In a device with the NbTiN slabs, the same four regions are measured, with a key difference being the apparent horizontal scaling of the Hall resistances for two regions adjacent to the NbTiN slabs. Longitudinal resistivity was measured from top contacts and bottom contacts for the regions 2 and 3 (red and green curves), and averaged

between the top and bottom pairing of regions 1 and 4 (black and blue curves) with the source and drain contact. These data were collected at a different electron density to accentuate the effect of the NbTiN slab's presence. All data were adjusted for magnet hysteresis (more information in the Supplemental Material [37]).

Two possible sources for the changes in the resistance versus $B$-field curves could include device inhomogeneity and transient effects. As a reaffirmation, all devices were checked for linearity in their zero-field current-voltage ($I$-$V$) responses (a set of which is available in the Supplemental Material [37]). After confirming this behavior, transient effects were analyzed by ramping the magnetic field in steps of 0.1 T while measuring the two resistances over a span of several time-constants corresponding to the equilibrating response. This resulted in a time-dependent resistance measurement and a parametric plot of the $B$-field-dependent resistance (both of which are in the Supplemental Material [37]). The effects of any transient phenomena were thus characterized and represented by an uncertainty that became applicable to all resistance measurements.

In Fig. 4 (a), several Hall resistances and electron densities were measured for both types of regions (with and without NbTiN slabs). The data taken in regions without the slabs are shown as dotted lines and labelled as *Actual*, indicating the lack of external effects on expected control measurements. For the corresponding regions adjacent to the slabs, data curves are plotted as solid curves labelled as *Apparent* with a shaded region indicating the 1σ uncertainty associated with electron density variation and transient effects. This shading is only presented for this graph to grant clarity in the remaining figures. The corresponding longitudinal resistances are shown in Fig. 4 (b) and verify the apparent scaling factor present within the regions near NbTiN slabs.

One may intuitively gather that a superconductor in the pure Meissner state (and to a smaller extent, a mixed state) would expel $B$-fields, possibly contributing to the apparent scaling. In Fig. 4 (c) and (d), temperature-dependent Hall resistance and longitudinal resistivity data for a fixed electron density were compared, respectively. The agreement of the *Actual* and *Apparent* data (within experimental uncertainty) for measurements at higher temperatures approaching $T_c$ suggests that the NbTiN superconducting state is contributing to the observed scaling.
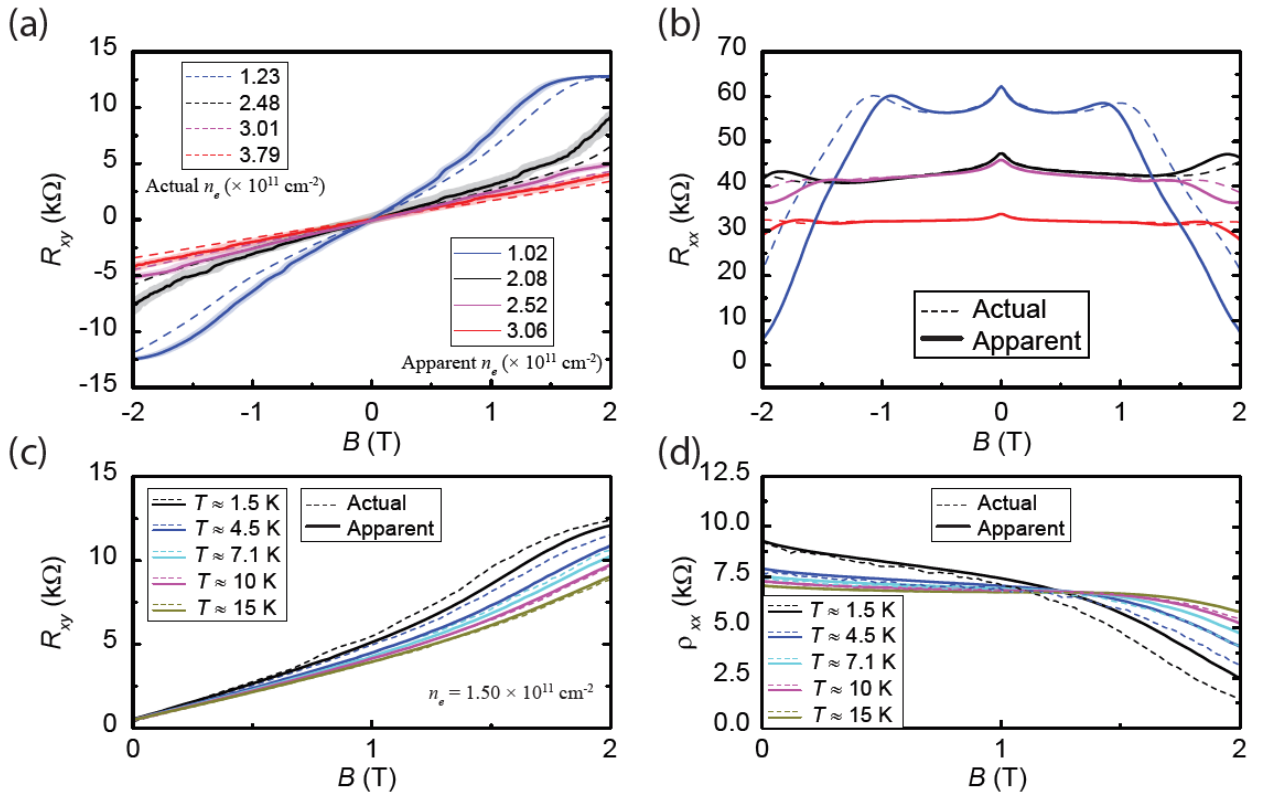


FIG. 4. (Color online) (a) Several Hall resistances were measured for regions with and without nearby NbTiN slabs. Data taken in regions without the slabs are shown as dotted lines (*Actual*). For corresponding regions adjacent to the slabs, data curves are shown as solid with a shaded region indicating the $1\sigma$ uncertainty associated with electron density variation and transient effects. (b) Longitudinal resistances were measured to verify the apparent scaling factor present within the regions adjacent to NbTiN slabs. (c) Hall and (d) longitudinal resistance data for one electron density were compared at several temperatures, with one being above $T_c$ for NbTiN.

## IV. ABRIKOSOV VORTEX CORRECTIONS

### A. Comparing Pure and Mixed States

To better quantify the aforementioned observations, Hall resistance data for a fixed electron density from regions with and without NbTiN slabs were compared to yield the fractional differences in Hall resistances (Fig. 5 (a)). The light blue region indicates the bounds of what we are calling low-field, since higher fields contribute nonlinearly to changes in the electron density. To calculate electron densities with low $B$-field resistance measurements, the $B$-field bounds are roughly $\pm 2$ T. In Fig. 5 (b), the difference in the *Actual* and *Apparent* responses yield an average "enhancement" factor of about 16.3%. This average was determined from low-field data and is labelled as an enhancement factor for consistency with what should be a stronger magnetic field near the NbTiN slabs. To understand the extent of this enhancement, another set of Hall resistance data was simulated by scaling the *Actual* data with the expected average magnetic field across the width of the device determined by the pure Meissner state case in Fig. 2 (d) and (e). All of these curves are shown in Fig. 5 (c), with the *Actual* and *Apparent* cases shown as gold and red curves, respectively, and the pure Meissner, simulated resistance curve shown as a dotted blue curve.

Another way to justify our low-field limitations to these analyses can be seen in Fig. 5 (d), (e), and (f). The first derivatives for each of three Hall resistance measurements at three fixed electron densities are shown, and though the flatness is not ideal, it is evident that the characteristic linearity of *Actual* data is only reliable for determining the electron density, and by extension, any clean contributions to local $B$-field enhancement, for $B$-fields within $\pm 1$ T. Nonetheless, one may continue to analyze low-field data for learning more about the contributions of Abrikosov vortices on the observed $B$-field enhancement.
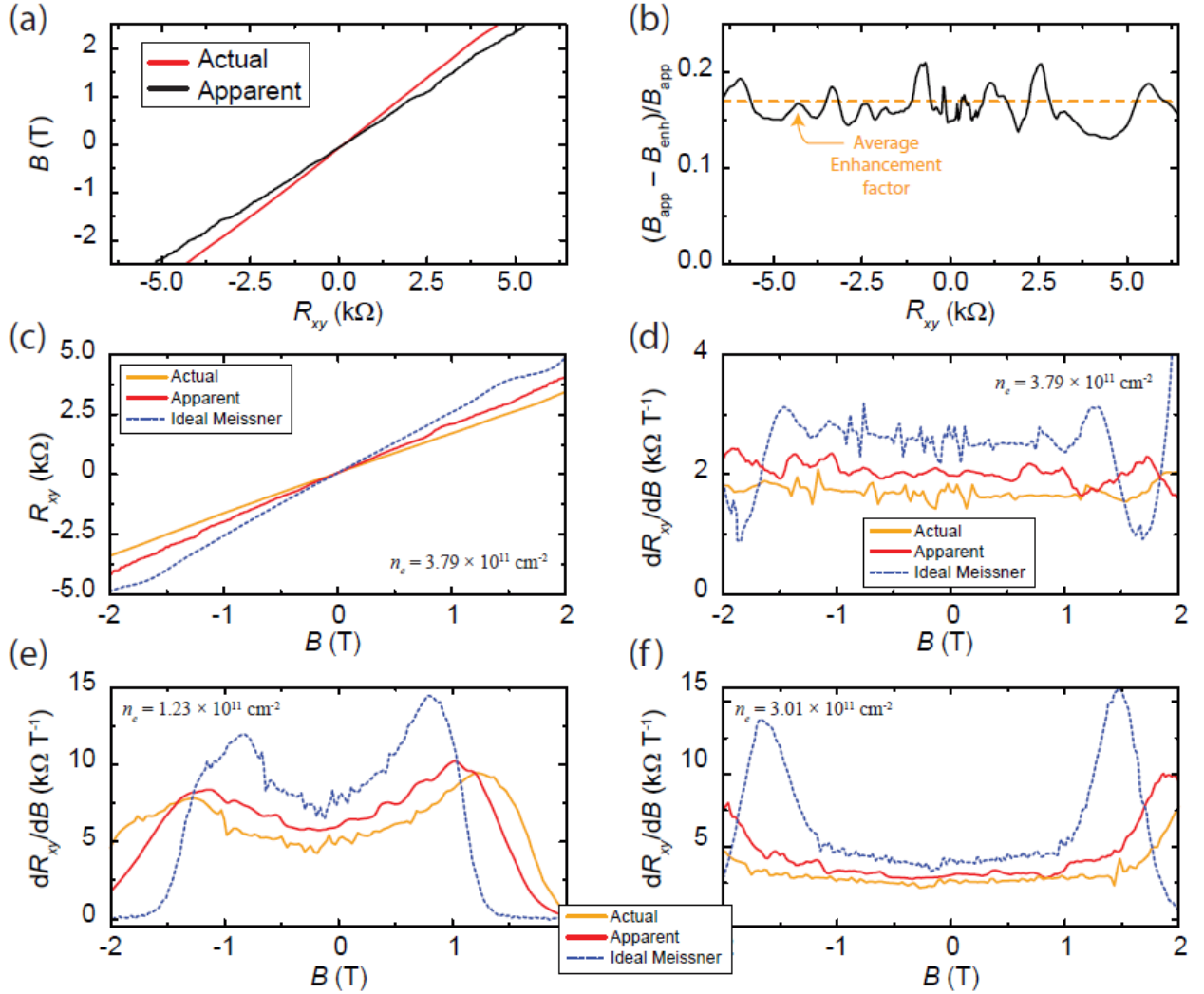
FIG. 5. (Color online) (a) Data for a fixed electron density are compared to yield the fractional difference observed in regions adjacent to NbTiN slabs. The light blue region indicates the maximum extent of the validity of approximating the electron densities with low $B$-field resistance measurements. (b) The difference in the *Actual* and *Apparent* responses yield an average enhancement factor of about 16.3%, determined from the low-field data. (c) Hall resistance data for a fixed electron density are compared for the *Actual* and *Apparent* cases (gold and red, respectively) as well as a simulated response curve for the event where the superconductors are in a pure Meissner state (dotted blue). (d), (e), and (f) The first derivative of the Hall resistance for three electron densities are shown to exhibit the extent of the validity of low-field electron density approximations.

## B. Vortex Contributions

To gain a better understanding for how Abrikosov vortices are behaving at low fields, and to attribute some density of vortices with our observations, we begin with the Ginzburg-Landau (GL) equations (Eqs. 2 and 3):

$$\frac{1}{2m}\left(\frac{\hbar}{i}\nabla - \frac{e}{c}\mathbf{A}\right)^2 \psi + \alpha\psi + \beta|\psi|^2\psi = 0$$

(2)

$$\mathbf{J} = \frac{c}{4\pi}\nabla \times \mathbf{B} = \frac{e\hbar}{2mi}(\psi^*\nabla\psi - \psi\nabla\psi^*) - \frac{e^2}{mc}\psi^*\psi\mathbf{A}$$

(3)

Within this discussion, we define all variables as such: $m$ (mass), $e$ (elementary charge), $c$ (speed of light), $\psi$ (wavefunction, with corresponding radial component $f$ and long-distance coefficient $\psi_\infty$), $\alpha$ and $\beta$ (phenomenological parameters), $\mathbf{J}$ (current density), $\mathbf{B}$ (magnetic field), $\mathbf{A}$ (vector potential), $\Phi_0$ (magnetic flux quantum). A vortex can be described by the following wavefunction: $\psi = \psi_\infty f(r)e^{i\theta}$. When used in conjunction with a nonsingular variation of the London gauge potential, simplifying the GL equations yields [46]:

$$f - f^3 - \xi^2\left[\left(\frac{1}{r} - \frac{2\pi A}{\Phi_0}\right)^2 f - \frac{1}{r}\frac{d}{dr}\left(r\frac{df}{dr}\right)\right] = 0$$

(4)

$$\mathbf{J} = \frac{e\hbar}{m}\psi_\infty^2 f^2\left(\frac{1}{r} - \frac{2\pi A}{\Phi_0}\right)$$

(5)

The reason for pointing out these formulations is because in many instances of discussing a vortex, one typically only concerns oneself with the $B$-field surrounding and far from the core (which has a radius of about $\xi$). For these cases, it is well-known that $f$ can be approximated as unity, and solving for Eqs. 4 and 5 yield a final vortex $B$-field of [47]:

$$\mathbf{B}(r) = \frac{\Phi_0}{2\pi\lambda^2}K_0\left(\frac{r}{\lambda}\right)$$

(6)

In Eq. 6, $K_0$ is a modified Bessel function of the second kind. To construct any arrangement of vortices, it is important to describe the *B*-field behavior in the core more accurately since a logarithmically diverging field at small distances is not realistic enough for our attributions. Thankfully, expressions for *f* have been derived for such small distances [47]:

$$f(r) \approx \frac{r}{2\xi}\left[1 - \frac{r^2}{8\xi^2}\left(1 + \frac{B(0)}{B_{c2}}\right)\right]$$

(7)

In this case, $B(0)$ comes from a fixed value near the center of the vortex ($r \to 0$), found once $\mathbf{A}(r)$ is known via: $\mathbf{A}(r) = \frac{1}{r}\int_0^r r'\mathbf{B}(r')dr'$. Equation 7, when substituted into Eqs. 4 and 5, enables one to numerically solve the more accurate form of $\mathbf{B}(r)$. This vortex field, specific to the NbTiN slabs, is plotted in the Supplemental Material [37], along with a short-range summation of periodic, neighboring vortices to demonstrate how these flux quanta, when arranged appropriately, allow a *B*-field ($B_{c2} > B > B_{c1}$) to penetrate the NbTiN slab. By taking the limit of summation in the case where the free energy of the vortex system is minimized [47, 48], we obtain a triangular lattice of spacing: $\left(\frac{4}{3}\right)^{1/4}\sqrt{\frac{\Phi_0}{B}}$ (which is also plotted in the Supplemental Material [37]).

One may now say that for a reasonably low field (less than 1 T), a triangular formation of Abrikosov vortices, with an inter-core distance lower bound of the order $10\xi$, reduces the impact of the Meissner effect on local *B*-field enhancement by a factor with a lower bound of approximately 2.5 to 3. This reduction is determined by taking the ratio of the horizontal scaling factors observed, one set of which is shown in Fig. 5 (c). The inclusion of flux pinning and defects are beyond the scope of this analysis, but it is understood that ideal case scenarios have inherent mathematical limitations. Though these observations have given an overall upper bound

to the effect of Abrikosov vortices on the changes in Hall resistance and longitudinal resistivity, the inherent physics behind the enhanced field should not change in the event that other superconductors are used. Observations with type I superconductors are warranted in future studies, despite critical temperatures being of mK order. Furthermore, for applications to other 2D materials, such as germanene, silicene, or phosphorene, appropriate experimental conditions must be established to measure the effect of any enhanced field, especially if a linear Hall effect at low $B$-field is not present in the material.

## V. CONCLUSIONS

In this work, we investigated the effects of enhanced $B$-fields resulting from adjacent type II superconducting NbTiN slabs on the magnetotransport physics of narrow Hall bar devices fabricated from EG. The observed apparent changes in the magnetoresistances were found to have minimal contributions from device inhomogeneities, magnet hysteresis, electron density variations along the devices, and transient phenomena. The mixed state in type II superconductors enabled the formation of Abrikosov vortices. When our determined $\lambda_L$ was coupled with elements of Ginzburg-Landau theory, an approximation of the vortex densities at low-field (below 1 T) became calculable. This analysis ultimately offered an upper bound to the effect of Abrikosov vortices on the changes in Hall resistance and longitudinal resistivity. The results and analyses presented here offer advancement in the application space of low-field, low-temperature technologies, where the local $B$-field enhancement is able to reduce future $B$-field requirements for a variety of devices.

REFERENCES

[1] A.K. Geim and K.S. Novoselov, Nat. Mater. **6**, 183 (2007).

[2] A.H. Castro Neto, F. Guinea, N. M. R. Peres, K. S. Novoselov, and A. K. Geim, Rev. Mod. Phys. **81**, 109 (2009).

[3] K.S. Novoselov, V.I. Fal'ko, L. Colombo, P.R. Gellert, M.G. Schwab, and K. A. Kim, Nature **490**, 192 (2012).

[4] S. Das Sarma, S. Adam, E.H. Hwang, and E. Rossi, Rev. Mod. Phys. **83**, 407 (2011).

[5] N. Tombros, C. Jozsa, M. Popinciuc, H. T. Jonkman, and B. J. Van Wees, Nature **448**, 571-4 (2007).

[6] S. Cho, Y. F. Chen, and M. S. Fuhrer. Appl. Phys. Lett. **91**, 123105 (2007).

[7] M. Ohishi, M. Shiraishi, R. Nouchi, T. Nozaki, T. Shinjo, Y. Suzuki, Jpn. J. Appl. Phys. **46**, L605 (2007).

[8] M. H. Liu, C. Gorini, and K. Richter. Phys. Rev. Lett. **118**, 066801 (2017).

[9] S. Ghosh and M. Sharma, J. Phys. Condens Mat. **21**, 292204 (2009).

[10] S. Chen, Z. Han, M. M. Elahi, K. M. Habib, L. Wang, B. Wen, Y. Gao, T. Taniguchi, K. Watanabe, J. Hone, A. W. Ghosh, Science **353**, 1522-5 (2016).

[11] T. Taychatanapat, K. Watanabe, T. Taniguchi, P. Jarillo-Herrero, Nat. Phys. **9**, 225-9 (2013).

[12] A. F. Rigosi, A. R. Panna, S. U. Payagala, M. Kruskopf, M. E. Kraft, G. R. Jones, B. Y. Wu, H. Y. Lee, Y. Yang, J. Hu, D. G. Jarrett, D. B. Newell, and R. E. Elmquist, IEEE Trans. Instrum. Meas. **68**, 1870-8 (2018).

[13] R. Ribeiro-Palau, F. Lafont, J. Brun-Picard, D. Kazazis, A. Michon, F. Cheynis, O. Couturaud, C. Consejo, B. Jouault, W. Poirier, and F. Schopfer, Nat. Nanotechnol. **10**, 965 (2015).

[14] J. Hu, A. F. Rigosi, M. Kruskopf, Y. Yang, B.-Y. Wu, J. Tian, A. R. Panna, H.-Y. Lee, S. U. Payagala, G. R. Jones *et al*., Sci. Rep. **8**, 15018 (2018).

[15] A. Tzalenchuk, S. Lara-Avila, A. Kalaboukhov, S. Paolillo, M. Syväjärvi, R. Yakimova, O. Kazakova, T.J.B.M. Janssen, V. Fal'ko, and S. Kubatkin, Nat Nanotechnol. 5, **186** (2010).

[16] A. F. Rigosi and R. E. Elmquist, Semicond. Sci. Technol. **34**, 093004 (2019).

[17] K. Komatsu, C. Li, S. Autier-Laurent, H. Bouchiat, S. Guéron, Phys. Rev. B **86**, 115412 (2012).

[18] S. Bhandari, G. H. Lee, K. Watanabe, T. Taniguchi, P. Kim, and R. M. Westervelt, Nano Lett. **20,** 4890-4 (2020).

[19] M. Popinciuc, V. E. Calado, X. L. Liu, A. R. Akhmerov, T. M. Klapwijk, L. M. Vandersypen, Phys. Rev. B **85**, 205404 (2012).

[20] F. E. Schmidt, M. D. Jenkins, K. Watanabe, T. Taniguchi, G. A. Steele, Nat. Commun. **9**, 1-7 (2018).

[21] H. J. Suominen, J. Danon, M. Kjaergaard, K. Flensberg, J. Shabani, C. J. Palmstrøm, F. Nichele, C. M. Marcus, Phys. Rev. B **95**, 035307 (2017).

[22] F. K. de Vries, T. Timmerman, V. P. Ostroukh, J. van Veen, A. J. Beukman, F. Qu, M. Wimmer, B. M. Nguyen, A. A. Kiselev, W. Yi, M. Sokolich, Phys. Rev. Lett. **120**, 047702 (2018).

[23] Commercial equipment, instruments, and materials are identified in this paper in order to specify the experimental procedure adequately. Such identification is not intended to imply recommendation or endorsement by the National Institute of Standards and Technology or the United States government, nor is it intended to imply that the materials or equipment identified are necessarily the best available for the purpose.

[24] M. Kruskopf, D. M. Pakdehi, K. Pierz, S. Wundrack, R. Stosch, T. Dziomba., M. Götz, J. Baringhaus, J. Aprojanz, and C. Tegenkamp, 2D Mater. **3**, 041002 (2016).

[25] V. Panchal, Y. Yang, G. Cheng, J. Hu, M. Kruskopf, C.-I. Liu, A. F. Rigosi, C. Melios, A. R. Hight Walker, D. B. Newell, O. Kazakova, and R. E. Elmquist, Nat. Commun. Phys. **1**, 83 (2018).

[26] A.F. Rigosi, N.R. Glavin, C.-I. Liu Y. Yang, J. Obrzut, H.M. Hill, J. Hu, H.-Y. Lee, A.R. Hight Walker, C.A. Richter, R.E. Elmquist, and D.B. Newell, Small **13**, 1700452 (2017).

[27] M. Kruskopf, A. F. Rigosi, A. R. Panna, D. K. Patel, H. Jin, M. Marzano, M. Berilla, D. B. Newell, and R. E. Elmquist, IEEE Trans. Electron Dev. **66**, 3973 (2019).

[28] M. Kruskopf, A. F. Rigosi, A. R. Panna, M. Marzano, D. Patel, H. Jin, D. B. Newell, and R. E. Elmquist, Metrologia **56**, 065002 (2019).

[29] A. A. Abrikosov, J. Phys. Chem. Solids **2**, 199-208 (1957).

[30] J. Bardeen, M. J. Stephen, Phys. Rev. **140**, A1197 (1965).

[31] K. Maki, J. Low Temp. Phys. **1**, 45-58 (1969).

[32] S. Sarkar, H. Zhang, J.-W. Huang, F. Wang, E. Bekyarova, C.N. Lau, and R.C. Haddon, Adv. Mater. **25**, 1131 (2013).

[33] E. Bekyarova, S. Sarkar, S. Niyogi, M.E. Itkis, and R.C. Haddon, J. Phys. D: Appl. Phys. **45**, 154009 (2012).

[34] A.F. Rigosi, M. Kruskopf, H.M. Hill, H. Jin, B.-Y. Wu, P.E. Johnson, S. Zhang, M. Berilla, A.R. Hight Walker, C.A. Hacker, D.B. Newell, and R.E. Elmquist, Carbon **142**, 468 (2019).

[35] S. Che, K. Jasuja, S.K. Behura, P. Nguyen, T.S. Sreeprasad, and V. Berry, Nano Lett. **17**, 4381 (2017).

[36] T.J.B.M. Janssen, A. Tzalenchuk, R. Yakimova, S. Kubatkin, S. Lara-Avila, S. Kopylov, et al. Rev B **83**, 233402 (2011).

[37] See Supplemental Material at [URL] for information on the upper critical field determination, layout of the COMSOL model, magnet hysteresis, device homogeneity, transient effects, electron density shifts with temperature, and vortex visualizations. Includes Ref. [49].

[38] N. R. Werthamer, E. Helfand, and P. C. Hohenberg, Phys. Rev. **147**, 295 (1966)

[39] A. Gurevich, Phys. Rev. B **67**, 184515 (2003).

[40] A. Klimov, W. Słysz, M. Guziewicz, V. Kolkovsky, I. Zaytseva, and A. Malinowski, Physica C Supercond. **536**, 35-8 (2017).

[41] M. N. Kunchur, Condens. Matter **4**, 54 (2019).

[42] N. S. Swails, (2018). Depairing current density in NbTiN superconducting films. (Doctoral dissertation). Retrieved from https://scholarcommons.sc.edu/etd/4918

[43] J.-G. Caputo, L. Gozzelino, F. Laviano, G. Ghigo, R. Gerbaldo, J. Noudem, Y. Thimont, and P. Bernstein, J. Appl. Phys. **114**, 233913 (2013).

[44] D. Y. Vodolazov and I. L. Maksimov, Physica C **349**, 125-38 (2001).

[45] E. A. Matute, Am. J. Phys. **67**, 786-8 (1999).

[46] Z. Tan, C. Tan, L. Ma, G. T. Liu, L. Lu, C. L. Yang, Phys. Rev. B **84**, 115429 (2011).

[47] M. Tinkham, Introduction to superconductivity. Courier Corporation; 2004.

[48] H. Kleiner, L. M. Roth, and S. H. Autler, Phys. Rev. **133**, A1226 (1964).

[49] C. W. Liu, C. Chuang, Y. Yang, R. E. Elmquist, Y.-J. Ho, H.-Y. Lee, and C.-T. Liang, 2D. Mater. **4**, 025007 (2017).

TABLE OF CONTENTS GRAPHIC (AT END OF DOC)